ORIGINAL PAPER

A generalized van der Pol nonlinear model of vortex-induced vibrations of bridge decks with multistability

Wei Cui · Lin Zhao · Yaojun Ge · Kun Xu

Abstract The mathematical model of vortex-induced vibrations (VIV) on long-span bridges is important to predict nonlinear structural responses. Such models can be divided into two categories: wake-oscillator and single-degree-of-freedom (SDOF) models. The SDOF model is widely used for wind-induced vibration calculations. However, the traditional SDOF model based on the standard van der Pol oscillator cannot simulate VIVs with multistability. In this study, a newly generalized van der Pol model is proposed to incorporate the limit-cycle oscillation (LCO) with multiple amplitudes, and the nonlinear damping is expressed by polynomial expansion. Next, the multiple LCO amplitudes can be determined from the energy evolution formula derived from the averaging method. Similarly, the evolution of the vibration amplitude during the transient response is also derived by the same method. Subsequently, nonlinear parameter identification methods based on constraint optimization are derived according to both the LCO amplitude and transient responses. In the last part of this study, the "energy map" is proposed to present the energy extracted from the fluid–structure interaction with different wind speeds and vibration amplitudes, and it is constructed by the parameters identified in the lock-in range of VIV. The "energy map" can provide a complete picture of the evolution of the energy of VIVs on bridge decks.

Keywords Vortex-induced vibration · Bridge deck · Dynamic stability · Multistability · Limit-cycle oscillation

W. Cui · L. Zhao (✉) · Y. Ge
State Key Lab of Disaster Reduction in Civil Engineering, Tongji University, 1239 Siping Road, Shanghai 200092, China
e-mail: zhaolin@tongji.edu.cn

W. Cui
e-mail: cuiwei@tongji.edu.cn

Y. Ge
e-mail: yaojunge@tongji.edu.cn

W. Cui · L. Zhao · Y. Ge
Key Laboratory of Transport Industry of Wind Resistant Technology for Bridge Structures, Tongji University, Shanghai, China

K. Xu
Key Laboratory of Urban Security and Disaster Engineering of Ministry of Education, Beijing University of Technology, 100 Pingleyuan, Beijing 02115, China
e-mail: xukun@bjut.edu.cn

1 Introduction

When fluids flow past a bluff body, periodic vortices are generated at the wake. Normally, the frequency of vortices is linearly proportional to the inflow velocity, and the proportional ratio is characterized by the Strouhal number $St = fD/U$, where f is the dominant frequency of the vortex shedding; D is the character dimension of the bluff body; and U is the mean incoming flow velocity [39]. When the frequency of vortex shedding is close to the structural vibration frequency, resonance between the structure and vortex occurs. This resonance is also known as vortex-induced

vibration (VIV). As the wind speed increases, the VIV amplitude increases dramatically, but the vortex frequency remains the same as the structural frequency and is captured by the structural motion; therefore, the vortex frequency does not increase as before. This phenomenon is known as "lock-in". As the wind speed further increases, the VIV amplitude decreases to 0, and the vortex frequency "lock-in" also disappears. The wind velocity range where vortex frequency "lock-in" and VIV occurs is named the "lock-in" range.

The mechanisms of VIVs, which contain rich and complex phenomena, are still not fully understood and are an active research field in both fluid mechanics and engineering. The mechanism of fluid–structure interactions has been extensively investigated in the field of fluid mechanics. The effects of the mass ratio and structural damping [30] and Reynolds number [32] on VIVs have been extensively studied. In recent years, the triggering mechanism of VIVs has been studied with linear stability analysis methods through direct numerical simulations [28] and reduced-order models [48], and two significant modes, namely, the "nearly structural" mode and a von Kármán "purely fluid" mode, have been identified.

VIVs also have wide applications in many engineering applications, such as long-span bridges, tall chimneys[31], long risers [46] and energy harvesters [47]. In recent decades, as the spans of bridges increase, the structural dynamic frequency decreases. Therefore, the effects of VIVs on long span suspension bridges are often reported around the world, such as in the Deer Isle bridge in the USA[19], the Great Belt bridge in Denmark [3,20], the Trans-Tokyo Bay crossing bridge in Japan [4], the Yi Sun-Sin bridge in Korea[15] and the Xihoumen bridge [6,21,22] and Humen bridge [49] in China. Due to self-limited features, the VIVs of a bridge generally does not cause damage to structural elements. However, VIVs adversely affect bridge operations and cause issues to vehicle drivers and pedestrians [7,40]. Therefore, VIVs have become the major concern of wind-induced vibrations on long-span bridges.

Because of the large aspect ratio (width-to-depth) of the bridge deck, the VIV mechanisms of a long-span bridge are clearly different in square and circular sections; this concept has been heavily studied in the field of fluid mechanics [44]. The mechanism of vortex-drifting and shedding [13] has been analyzed from the perspective of time-frequency evolutionary characteristics [11]. For bridge sections with twin boxes, the vor-

tex motion in the central slotting is found to be the reason for VIVs on the Xihoumen Bridge[21,22]. Many countermeasures have been developed from an aerodynamic perspective [12,37,41] and mechanical systems [38,43,45].

Because of aerodynamic nonlinearity, structural vibration also has clear nonlinear features, such as motion-dependent dynamic characteristics and limit-cycle oscillation (LCO). The amplitude of LCOs in the "lock-in" range depends on wind speeds. To model the nonlinear dynamics during the VIV "lock-in" range, several nonlinear dynamic models have been developed. There are two categories of VIV dynamic models: wake-oscillator models and single-degree-of-freedom models. The wake-oscillator model considers the vortex wake as an extra self-vibrating body, interacting with the oscillator at the wake area. The most famous models are Hartlen-Currie's lift oscillator model [10] and the Iwan-Blevins early wake model [16]. Later, [34] proposed a physics-based nonlinear model to fully capture the nonlinear properties of VIVs, such as the limit cycle and multistability. The SDOF model is also popular, especially in engineering applications, because it is easy to implement. The SDOF model incorporates the vortex-induced force as the nonlinear aerodynamic forces dependent on structural motion. The most famous SDOF model is Scanlan's nonlinear VIV model [2], which uses a quadratic term to modify aerodynamic damping; thus, this model is equivalent to the van der Pol oscillator [29,36]. The van der Pol oscillator-based model was also generalized to include complex nonlinear mechanical damping [18]. [9] proposed several SDOF models to predict the VIV responses that can match the high-fidelity CFD numerical simulation. The SDOF model was also employed to evaluate the dynamic stability of the energy harvester.

In recent years, as an increasing number of long-span bridges are vulnerable to VIVs, the simple mathematical format of the SDOF model attracted the attention of scholars, and several other VIV models have been developed, including the Rayleigh oscillator model [42]. The performance of the difference VIV model was compared in [44]. The coefficient calibration of the VIV model is also important in engineering applications. Professor Tamura suggested that the coefficients should be derived based on a physical interpretation. However, it is also difficult to derive all coefficients when the nonlinear dynamic system becomes complex. Therefore, many coefficient regression methods, such

as direct aerodynamic measurements [5] and curve fitting through instantaneous aerodynamic damping and stiffness [44], have also been developed.

For a bridge with a complex deck shape, the aerodynamic nonlinearity becomes stronger, and multistable states of VIVs may appear. An open section deck, which was used for a medium-span cable-stayed bridge, was reported in [42] to have more than one stable state at a certain wind velocity. Tamura's wake-oscillator model in [34] can predict the multistability of VIVs; however, its derivation is based on a circular cylinder, and this method is not feasible for bridge decks with complex geometries. Scanlan's SDOF model, which is a standard van der Pol oscillator, has only one stable state. VIV multistability only occurs for the ascending stage or descending stage. The occurrence of multistability is related to the flow field modes during fluid–structure interaction. The VIV-favored flow field will only be excited with sufficient structural vibration amplitude; if the amplitude is small, both the VIV-prone flow field and the vibration will decay.

In this study, a generalized van der Pol oscillator is proposed to simulate VIVs with multistability. The equilibrium states of the proposed model are derived based on the energy averaging method, and the stability of each equilibrium state is discussed in detail. To calibrate the VIV model parameters with multiple stabilities, a model coefficient identification method is also proposed by employing the constraint optimization algorithm with known stable states as the constraint and the transient vibration before the stable state as the optimization object. Finally, the "energy map" is developed from the identified VIV model to demonstrate the evolving directions of the structural response throughout the VIV lock-in region. The wind tunnel testing results for a sectional bridge model are used to demonstrate the performance of the proposed VIV model and the identification procedure of the associated coefficients. It should be noted that although the proposed model is validated for the bridge section, it can also be applied to other structural types that have multiple stabilities during VIVs.

2 SDOF nonlinear vortex-induced vibration model based on a generalized van der Pol oscillator

The proposed mathematical formulation for nonlinear VIV is

$$m\frac{d^2x}{dt^2} + c\frac{dx}{dt} + kx$$

$$= \rho U^2 D\left[Y_1\left[1 - h\left(\frac{x}{D}\right)\right]\frac{\frac{dx}{dt}}{U}\right.$$

$$\left. + Y_2\frac{x}{D} + \frac{1}{2}C_L\sin(\omega_v t + \phi)\right] \qquad (1)$$

where x is the vibration amplitude; m-c-k are the structural mass, damping and stiffness, respectively; ρ is the air density; U is the wind speed; Y_1 is the velocity-dependent flutter derivative; Y_2 is the motion-dependent flutter derivative; $h\left(\frac{x}{D}\right)$ is a polynomial function of $\frac{x}{D}$ that quantifies nonlinear aerodynamic damping terms for Y_1; C_L is the lift coefficient amplitude; and ω_v is the vortex shedding frequency. Normally, ω_v is determined by its Strouhal number S_t as $2\pi\frac{S_t U}{D}$. ϕ is the phase difference between a vortex-induced force and vibration.

The nondimensional form of the model consisting of Eq. (1) is

$$\frac{d^2y}{ds^2} + 2\xi K_s\frac{dy}{ds} + K_s^2 y$$

$$= m^*\left[Y_1\left[1 - h(y)\right]\frac{dy}{ds} + Y_2 y\right.$$

$$\left. + \frac{1}{2}C_L\sin(2\pi S_t s + \phi)\right] \qquad (2)$$

where y is the nondimensional motion $y = x/D$, ξ is the damping ratio, K_s is the reduced structural frequency $K_s = \sqrt{\frac{k}{m}}\frac{D}{U}$, m^* is the mass ratio $m^* = \rho D^2/m$, and s is dimensionless time $s = U\frac{t}{D}$.

This equation can be rewritten as a modified van der Pol oscillator with periodical external forcing as follows:

$$\frac{d^2y}{ds^2} + \left[(2\xi K_s - m^*Y_1) + m^*Y_1 h(y)\right]$$

$$\frac{dy}{ds} + \nu^2 y = \frac{m^*}{2}C_L\sin(2\pi S_t s + \phi) \qquad (3)$$

in which $\nu^2 = K_s^2 - m^*Y_2$. Normally, the external vortex-shedding effects $\frac{m^*}{2}C_L$ (in the order of 10^{-5})

are much smaller than the self-excited force $2\xi K_s$ (in the order of 10^{-3}) for the bridge VIV response; thus, the term on the right side of the above equation can be dropped [2,5]. The omission of $\frac{m^*}{2}C_L$ may introduce response prediction errors when vibration amplitudes is small, but it will not affect the LCO amplitudes when VIV is stable. For other bluff bodies, external excitations are necessary for large mass ratios. To further simplify the above equation, one extra normalization $\eta = \nu^2 y = \nu^2 x/D$ and $\tau = \nu s$ is performed to modify the frequency of the above oscillator as unitary.

The final reduced form of the modified van der Pol oscillator is expressed as follows:

$$\ddot{\eta} + \epsilon\left[1 + g(\eta)\right]\dot{\eta} + \eta = 0 \tag{4}$$

where $\epsilon = \dfrac{2\xi K_s - m^* Y_1}{\nu}$. $\dot{\eta}$ indicates the differentiation of η with respect to the dimensionless time $\tau = \nu U \dfrac{t}{D}$. It should be noted that if the nonlinear aerodynamic damping function $h(y)$ is expressed as $h(y) = \sum_{i=1}^{N} a_i y^i$, then the normalized damping function is $g(\eta) = \sum_{i=1}^{N} b_i \eta^i$ where $b_i = a_i \dfrac{m^* Y_1}{\epsilon \nu^{2i}}$.

3 Theoretical calculation the limit-cycle amplitude of the generalized van der Pol oscillator

3.1 Amplitude of limit-cycles

Based on the nonlinear dynamic model in Eq. (4), the amplitude of the limit-cycle oscillation is derived from an energy evolution perspective. The total energy E is the sum of the potential energy and the kinetic energy.

$$E = \frac{1}{2}\eta^2 + \frac{1}{2}\dot{\eta}^2 \tag{5}$$

The energy evolution rate $\dot{E}$ is expressed as:

$$\dot{E} = \frac{dE}{d\tau} = \eta\dot{\eta} + \dot{\eta}\ddot{\eta} = -\dot{\eta}^2\epsilon\left[1 + g(\eta)\right] \tag{6}$$

Because normally $|\epsilon| \ll 1$, the generalized van der Pol oscillator model of VIVs is a weakly nonlinear damped dynamic system. Thus, the solution to Eq. (4) can be considered a sinusoidal function with a small perturbation [33].

$$\eta = A\cos(\tau + \phi) + o(\epsilon) \tag{7a}$$

$$\dot{\eta} = -A\sin(\tau + \phi) + o(\epsilon) \tag{7b}$$

where A is the limit cycle amplitude to be determined, ϕ is the phase angle, and $o(\epsilon)$ is the small perturbation of the sinusoidal function of the order of ϵ. Now, the changes in the energy E in one period are

$$\Delta E = \int_0^{2\pi} \frac{dE}{d\tau}d\tau$$
$$= -\epsilon \int_0^{2\pi} \dot{\eta}^2\left[1 + g(\eta)\right]d\tau + o(\epsilon^2) \tag{8}$$

Expanding $g(\eta)$ as polynomials in the above equation yields:

$$\Delta E = -\epsilon \int_0^{2\pi} A^2 \sin^2(\tau + \phi)$$
$$\left[1 + \sum_{i=1}^{N} b_i A^i \cos^i(\tau + \phi)\right]d\tau + o(\epsilon^2) \tag{9}$$

$o(\epsilon^2)$ is a second-order small number and can be dropped. Because it is a weakly nonlinear dynamic system, the amplitude can be considered a constant during one period integral, and the phase angle ϕ effect is averaged over one period. Therefore, the final formula for the energy changes ΔE is

$$\Delta E = -\epsilon A^2 \left(I_0 + \sum_{i=1}^{N/2} b_{2i} I_{2i} A^{2i}\right) \tag{10}$$

where I_i is the definite integral $\int_0^{2\pi} \sin^2\tau \cos^i\tau\, d\tau$ for $i = 0, 1, 2, 3,\ldots$ However, $I_i = 0$ if i is odd; thus, only terms with i as even are contained in Eq. (10). $I_0 = \pi$ and by the Wallis formula, $I_i = \dfrac{i-1}{i+2}I_{i-2}$ if i is even.

When the dynamic system enters the limit-cycle oscillation, $\Delta E = 0$. Since $A = 0$ is trivial, the amplitude A should satisfy the following equation:

$$I_0 + \sum_{i=1}^{N/2} b_{2i} I_{2i} A^{2i} = 0 \tag{11}$$

It should be noted that only the root that satisfies $A^2 \geq 0$ has physical meaning; if $A^2 < 0$, the amplitude will be a virtual number and not discussed here. For a standard van der Pol oscillator $b_i = 0$, except $b_2 = 1$ and ϵ are small negative numbers, the amplitude of a standard van der Pol oscillator is $A = 2$ [35,36].

3.2 The stability of limit-cycles

When $A = 0$, ΔE is also 0; thus, $A = 0$ is a neutral equilibrium point. When A^2 is small, the dynamic system is linear, and the energy change is $\Delta E \approx -\epsilon A^2 I_0$. Moreover, the energy changes near the origin are determined by the sign of ϵ: when $\epsilon > 0$, the energy decays, while when $\epsilon < 0$, the energy gains. Similarly, when A^2 is large, nonlinear damping starts to take effect, and therefore, the system will be discussed separately for $\epsilon > 0$ and $\epsilon < 0$.

For a nonlinear dynamic system containing one stable and one unstable limit cycle, it is sufficient to expand $g(\eta)$ to the 4th-order; thus, N in Eq. (10) and Eq. (11) is set to 4 in this study. The minimum order N of polynomials should be at least double the number of stabilities observed during VIVs. For example, if there is an extra unstable or stable limit-cycle, $g(\eta)$ should be expanded to the 6th-order. Furthermore, the polynomial expansion order N also needs to consider the fitness of the energy change rate results from wind tunnel tests. The roots of Eq. (11) are noted as A_1^2 and A_2^2, and it is supposed that $A_2^2 > A_1^2$. There are three situations for a different combination of A_1^2 and A_2^2. For $\epsilon < 0$, the dynamic system energy gains for a small amplitude A, and the behavior of the system will be up-side-down symmetric to the case $\epsilon > 0$.

■ $\epsilon > 0$

- $A_2^2 > A_1^2 > 0$: the energy change ΔE vs. squared amplitude A^2 is plotted in Fig. 1a). When $A^2 < A_1^2$, the energy in the dynamic system decays, and the oscillator converges to 0. When $A_1^2 < A^2 < A_2^2$, the energy gains, and the oscillator converge to A_2. When $A_1^2 < A^2 < A_2^2$, the energy also decays, and the oscillator converges to A_2.
- $A_2^2 > 0 > A_1^2$ (Fig. 1b): A_2^2 is the only valid solution to Eq. (11). When $A^2 < A_2^2$, the energy decays, and the oscillator converges to 0; when $A^2 > A_2^2$, the energy gains, and the oscillator diverges.
- $0 \geq A_2^2 \geq A_1^2$, or A_1^2 and A_2^2 are complex numbers (Fig. 1c): There is no valid solution to Eq. (11) and the equilibrium point. For all A, the energy always decays, and the oscillator converges to 0.

■ $\epsilon < 0$

- $A_2^2 > A_1^2 > 0$ (Fig. 1d): A_1^2 is the supercritical critical point, and A_2^2 is the subcritical critical point.
- $A_2^2 > 0 > A_1^2$ (Fig. 1e): A_2^2 is the only critical point, and it is supercritical bifurcation. It should be noted

that this is the most common VIV situation, and all A converge to the VIV amplitude A

- $0 \geq A_2^2 \geq A_1^2$, or A_1^2 and A_2^2 are complex numbers (Fig. 1f): There is no equilibrium point. For all A, the oscillator will diverge.

It should be noted that the six scenarios shown in Fig. 1 are just possible mathematical solutions to Eq. (11), and not every solution necessarily has a physical meaning.

The instability in Fig. 1b, d, f corresponds to the galloping of bluff bodies, which normally cannot be observed during the VIV wind tunnel test but shows the potential ability of the proposed generalized van der Pol model. Furthermore, there might be extra stable equilibrium points at larger A^2, and higher-order polynomials ($N \geq 6$) are required to capture their aerodynamic nonlinearity.

4 Aerodynamic coefficient determination in the proposed VIV model

The analysis of Eq. (10) shows that the evolution of the VIV amplitude can be separated into two parts: the transient part and the stationary part. In the stationary part, $\Delta E = 0$. The amplitude at the stationary part is noted as A_*, then the coefficients b_{2i} must satisfy the relationship of $f(A_*^2) = 0$:

$$I_0 + \sum_{i=1}^{N/2} b_{2i} I_{2i} A_*^{2i} = 0 \tag{12}$$

In the second part, the transient part will be used to determine the coefficients in Eq. (10), such as normalized linear damping ϵ.

When the oscillator reaches its maximum displacement (or minimum displacement), its velocity is 0. The dynamic system energy only contains the potential energy, and the kinetic energy is 0. Therefore, at the time step $\hat{\tau}$, the oscillator reaches its maximum amplitude $\hat{\eta}$, $A(\hat{\tau}) = \hat{\eta}(\hat{\tau})$. The energy of the dynamic system at $\hat{\tau}$ is expressed as

$$E(\hat{\tau}) = \frac{1}{2}\hat{\eta}^2 \tag{13}$$

After one period, the amplitude reaches its maximum again as $\hat{\eta} - \Delta\hat{\eta}$; therefore, the energy changes during one period are

$$\Delta E = \frac{1}{2}\hat{\eta}^2 - \frac{1}{2}(\hat{\eta} - \Delta\hat{\eta})^2 = \frac{1}{2}(2\hat{\eta} - \Delta\hat{\eta})(\Delta\hat{\eta}) \approx \hat{\eta}\Delta\hat{\eta} \tag{14}$$
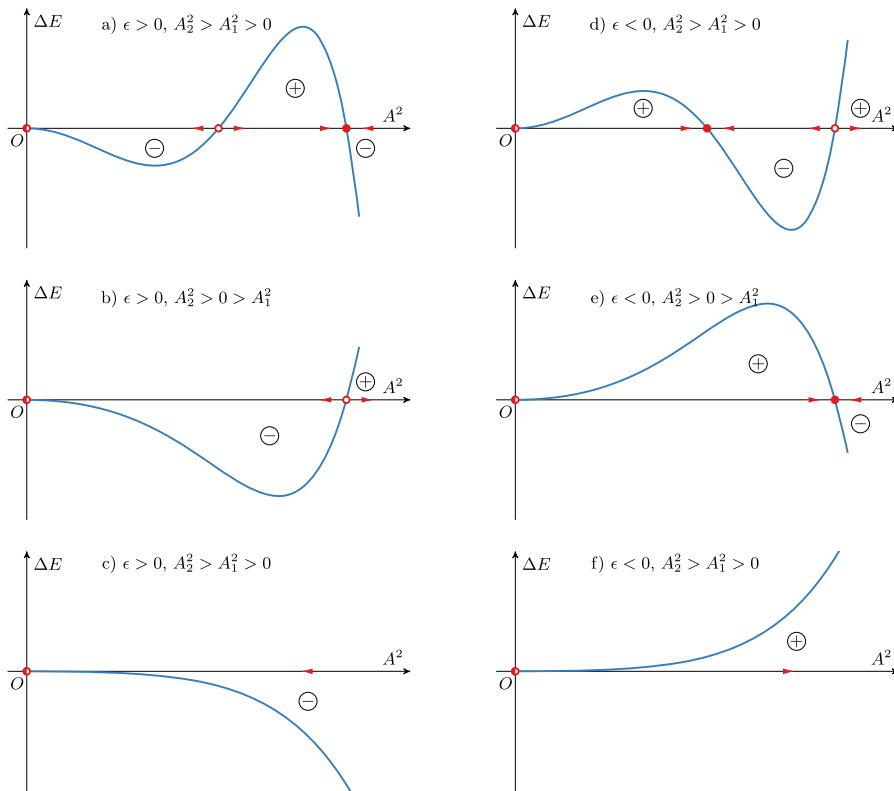
Fig. 1 Stability of equilibrium points for the VIV model with multiple limit-cycles (legends: ○, unstable equilibrium point; ●, stable equilibrium point; ◑, neutral equilibrium point; ⊖, energy decays; ⊕, energy gains;). (Color figure online)

since $\Delta^2 \hat{\eta}$ is a second-order small number and omitted here. On the other hand, the changes in energy during one period are already known in Eq. (10):

$$\Delta E = \hat{\eta}\Delta\hat{\eta} = -\epsilon\hat{\eta}^2 \left(I_0 + \sum_{i=1}^{N/2} b_{2i} I_{2i} \hat{\eta}^{2i} \right) \qquad (15)$$

The above formula is equivalent to the Lyapunov exponent [8], which can be used to determine the stability of the limit cycle. A similar method was also developed in [17] with improved stability characterization for aeroelastic energy harvesters. During the transient signal of VIVs, all coefficients can be determined by minimizing the residuals of the norm of Eq. (15)

$$\left| \Delta\hat{\eta} + \epsilon\hat{\eta} \left(I_0 + \sum_{i=1}^{N/2} b_{2i} I_{2i} \hat{\eta}^{2i} \right) \right|$$

The $\hat{\eta}$ for each signal can be computed by the absolute value of the Hilbert transformation of the vibration time series η.

In the last step, when converting the normalized VIV equation in Eq. (4) to the dimensional format in Eq. (1),

ν is required and can be identified by the predominant frequency of the VIV signal. After all, the aerodynamic coefficient determination procedure is summarized in five steps:

(1) Separation of the VIV signal into the stationary part and transient part.
(2) The envelope of the VIV signal is produced by the Hilbert transformation.
(3) Optimization:

$$\arg \min_{\epsilon, b_{2i}} \left| \Delta\hat{\eta} + \epsilon\hat{\eta} \left(I_0 + \sum_{i=1}^{N/2} b_{2i} I_{2i} \hat{\eta}^{2i} \right) \right|,$$

$$\text{subject to: } I_0 + \sum_{i=1}^{N/2} b_{2i} I_{2i} A_*^{2i} = 0; \qquad (16)$$

(4) ν is determined by the predominant frequency of the vibration signal.
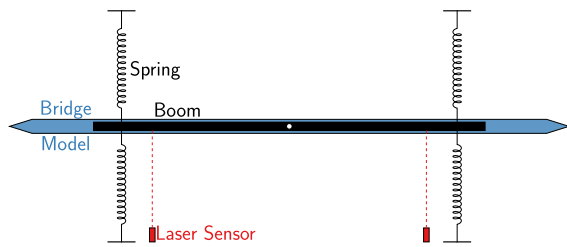(5) Converting normalized coefficients to dimensional coefficients.

Fig. 2 Schematic plot of the suspended sectional model

5 Experimental application of generalized van der Pol oscillator model

5.1 Sectional model wind tunnel test

The wind tunnel test was carried out in the TJ-2 wind tunnel of Tongji University, which is a closed-circuit wind tunnel with a test section that is 3 m wide and 2.5 m high. The operational airflow velocity is 2–68 m/s.

A bridge deck with two edge girders is employed as the prototype in this study. This bridge girder section is widely used in cable-stayed bridges with spans smaller than 500 m. The length scale of the sectional model is 60:1 to ensure that the wind tunnel blockage ratio is less than 2%.

The width, height, and length of the sectional model are 559.3 mm, 44.9 mm, and 1740 mm, respectively. The total mass including the model, boom and spring (elongated part) is 18.2 kg, the vertical vibration frequency f_n of the suspension system, shown in Fig. 2, is 3.37 Hz, and the logarithmic damping is $\xi = 4.7\text{\textperthousand}$. The linear mechanical damping assumption is used in this study because [23] demonstrated that the damping dependence on the vibration amplitudes in suspension systems is insignificant. Because only vertical VIVs are considered, the rotational inertia and frequency are not reported in this study.

Four laser displacement sensors are placed at two ends of the suspension boom to measure the wind-induced vibration signal of the bridge section during VIVs. The detailed geometry information is plotted in Fig. 3b, and the view of the sectional model in the TJ-2 wind tunnel is shown in Fig. 3a.

It should be noted that the dynamic system of the suspended bridge deck can only simulate 1-DOF VIVs, and the dynamic motion shape is uniform along the deck model. The actual long-span bridge contains multiple modes with close-spaced frequency, and the

(a) Sectional model in the TJ-2 wind tunnel
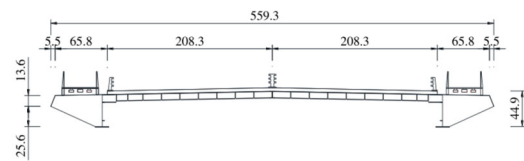
(b) Geometry of Sectional model (units: mm)

Fig. 3 Bridge deck sectional model tested in wind tunnel

dynamic model shapes are not uniform along the bridge span. However, the 2D VIV model proposed in this study can be applied to an actual long-span bridge based on the 2D flow assumption [1].

5.2 VIV characteristics for different wind speeds

The stable LCOs of VIV amplitudes for different wind speeds was obtained by a wind tunnel test, and the LCO amplitudes versus wind speeds are shown in Fig. 4. First, the sectional model was tested without manual disturbances. The VIVs of the bridge model was measured by increasing the wind speeds first, and then the lock-in region was retested by decreasing the wind speeds. The amplitudes of VIVs for increasing U and decreasing U are the same except for $U/f_n D = 8.59$. When U is increasing, the VIV amplitude is 0; however, when U is decreasing, the sectional section was stabilized at the same reduced wind speed $U/f_n D = 8.59$ with an amplitude of approximately 4.2 mm. From the first wind speeds of the occurrence of the VIVs, the Strouhal number is estimated as St $= f_n D/U = 0.116$.
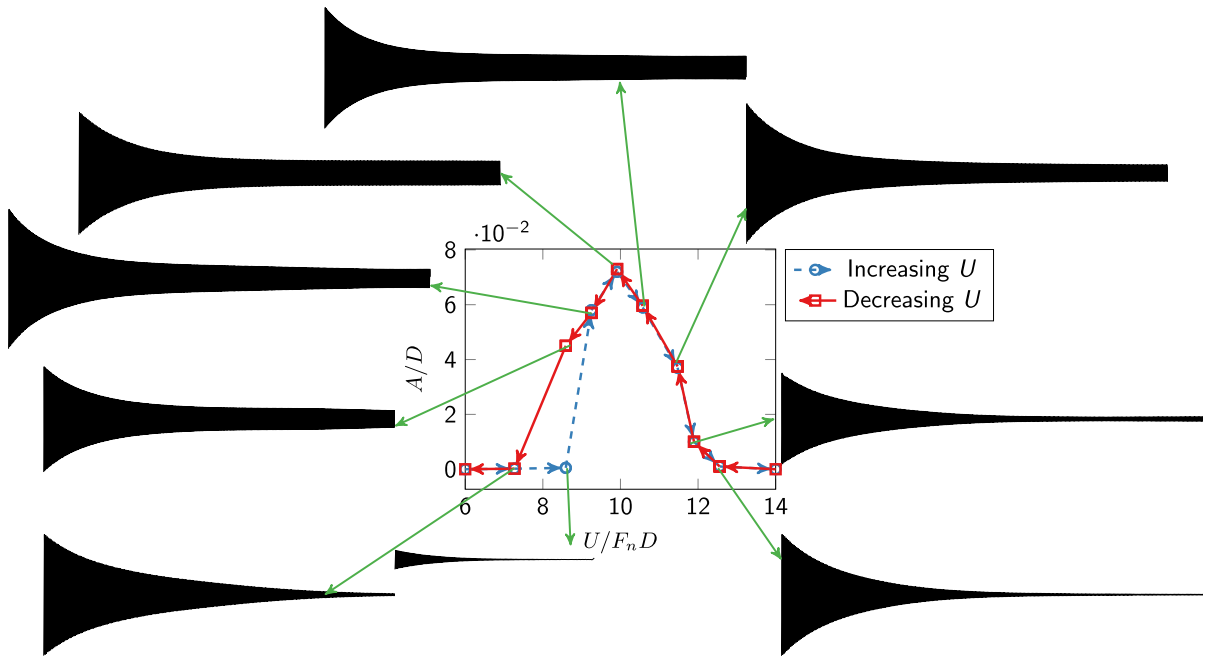
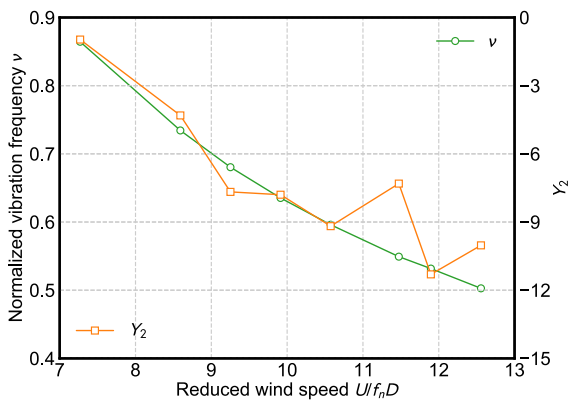**Fig. 4** Vibration characteristics of VIVs during the lock-in region

Fig. 5 Normalized vibration frequency ν and aerodynamic stiffness Y_2

Fig. 6 Dimensionless normalized LCO amplitude

The predominant frequency ν of each vibration displacement signal is identified and plotted in Fig. 5. The difference between the vibration frequency and the dynamic frequency of the sectional suspension system provides the aerodynamic stiffness parameters Y_2. The fluctuating value of aerodynamic stiffness at wind velocities higher than 11 m/s is because of the measuring errors at small amplitudes. Next, the normalized amplitude can be determined and plotted in Fig. 6.

To obtain the transient process approaching the VIV-LCO amplitude, the sectional model was disturbed and then approached different LCO amplitudes. The decay-to-resonance displacement signal was recorded for various wind speeds during the lock-in region and is also shown in Fig. 4. The stable VIV amplitudes are numerically labeled in Roman numbers. It clearly shows that at $U/f_n D = 8.59$, for a large initial disturbance, the model will decay to the VIV-LCO amplitude similarly to the decreasing scenario U. In contrast, for a small
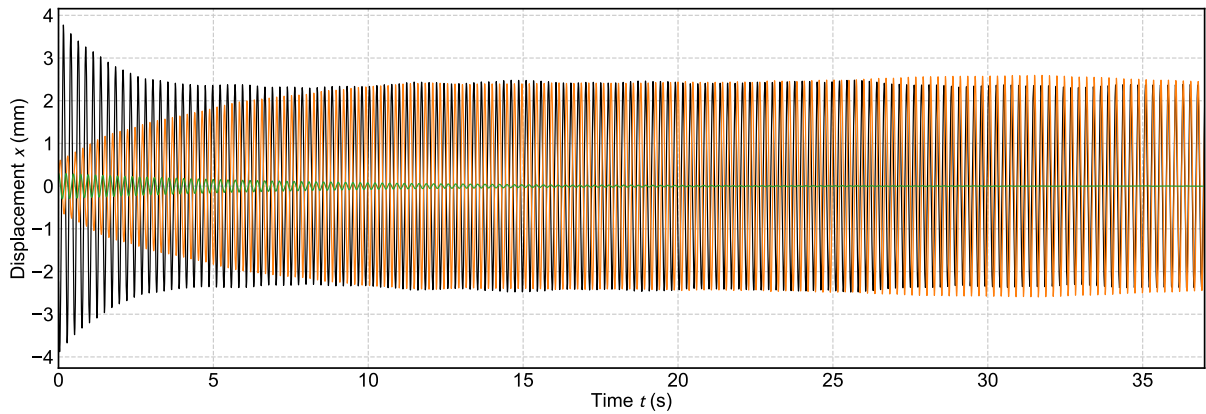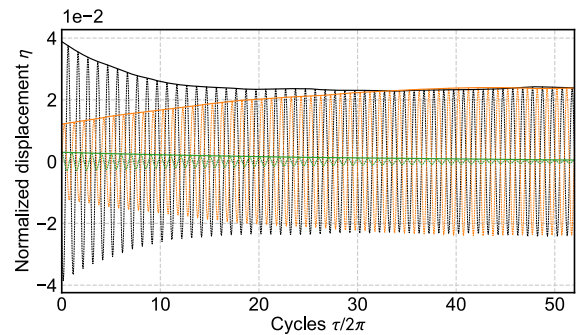
Fig. 7 Three different approaches to the stable state for a dynamic system depending on the initial amplitude when $U/f_n D = 8.59$
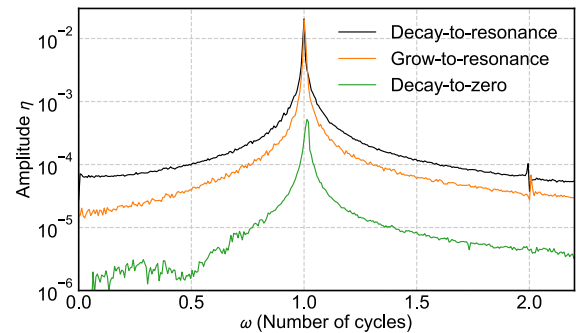
initial disturbance, VIVs will not occur, and the model will decay to 0 as the scenario increases U.

In summary, for $U/f_n D = 8.59$, there are two stable states for the bridge model: one is VIVs with an amplitude of 4.2 mm, and the other is 0 without VIVs. The original Scanlan SDOF VIV model assumes that the linear part of aerodynamic damping must exceed structural damping; in other words, $\epsilon < 0$ in Eq. (4) to make the dynamic system self-excitable.

An additional test at $U/f_n D = 8.59$ was performed with a slightly larger initial amplitude than in the decay scenario; however, this time, the model did not decrease but increased to the same amplitude as in a previous decay-to-resonance scenario. The three test results are shown in Fig. 7. There must be another equilibrium point that is, however, unstable. Therefore, the bridge model repels from this equilibrium point in two directions. When the initial amplitude is smaller than this equilibrium point, it will decay to 0; the whole initial amplitude is larger than this equilibrium point, and the model will be excited as LCOs. In summary, when $U/f_n D = 8.59$, the relationship between the changes in energy ΔE and the amplitude A of the dynamic system corresponds to the plots in Fig. 1a.

5.3 Coefficient identification of the generalized van der Pol model

Taking $U/f_n D = 8.59$ as an example, ν is identified as 0.9032 from the predominant frequency of the VIV vibration signal. After normalization, the VIV vibration data are plotted in the time domain and the frequency

(a) Time domain

(b) frequency domain

Fig. 8 Normalized VIV displacement of the bridge deck for $U/f_n D = 8.59$ with two stable states

domain in Fig. 8a, b, respectively. Figure 8b clearly shows that the vibration frequency of the normalized displacement η is 1. Figure 8b also demonstrates the high-order hormonic components, of which the amplitudes is highly depressed at the responses. The high-order hormonic components of vortex-induced force
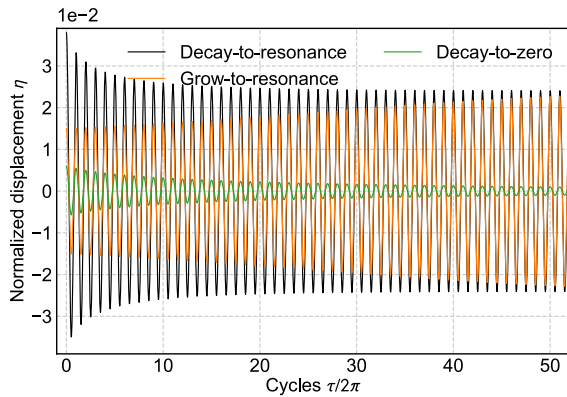
Fig. 9 Simulated VIV displacement on the bridge deck for $U/f_n D = 8.59$ with identified parameters

is more clear[5]. The amplitude envelope $\hat{\eta}$ calculated from the Hilbert transformation is plotted as the solid line for three scenarios with different initial amplitudes. The stable LCO amplitude A_* is 0.024 in Fig. 8b.

Substituting A_* as the optimization constraint and $\hat{\eta}$ as the optimization object in Eq. (16), the unknown parameters ϵ and b_i can be determined by a conventional optimization program, such as *fmincon* in MAT-LAB. Based on the identified parameters, the VIV vibration of the bridge can be simulated by a numerical integral algorithm for ordinary differential equations, and the results are plotted in Fig. 9.

5.4 Dynamic stability from an energy perspective

Based on the parameters identified and the nonlinear dynamics equation in Eq. (4), the vibration trajectories with the different initial conditions are simulated and plotted as phase portraits in Fig. 10a. It clearly shows that when the initial amplitude is above the stable LCO, the trajectory approaches the stable LCO; when the initial amplitude is below the unstable LCO, the trajectory moves away from the unstable LCO and approaches 0; when the initial amplitude is above the unstable LCO but below the stable LCO, the trajectory also moves away from the unstable LCO but in the opposite direction toward the stable LCO. The trajectory moving direction for different dynamic states is plotted in Fig. 10a.
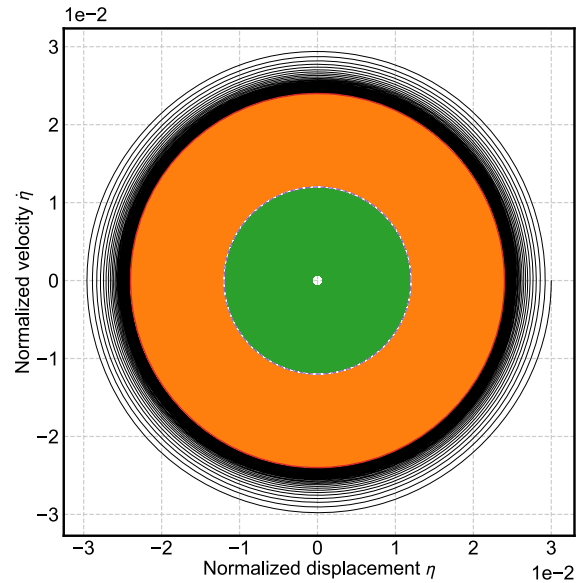
(a) Simulation
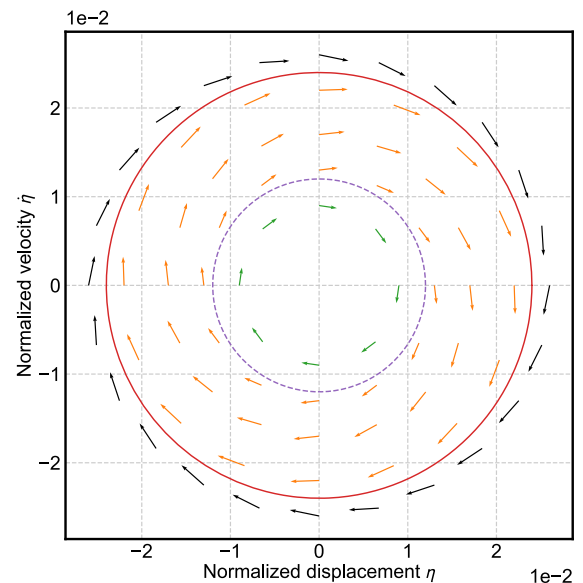
(b) Quiver plot

Fig. 10 Phase Portrait of the VIV response on the bridge deck for $U/f_n D = 8.59$ (Legend: —: decay-to-resonance; —: grow-to-resonance; —: decay-to-zero; —: Stable LCO; - · -: Unstable LCO). (Color figure online)
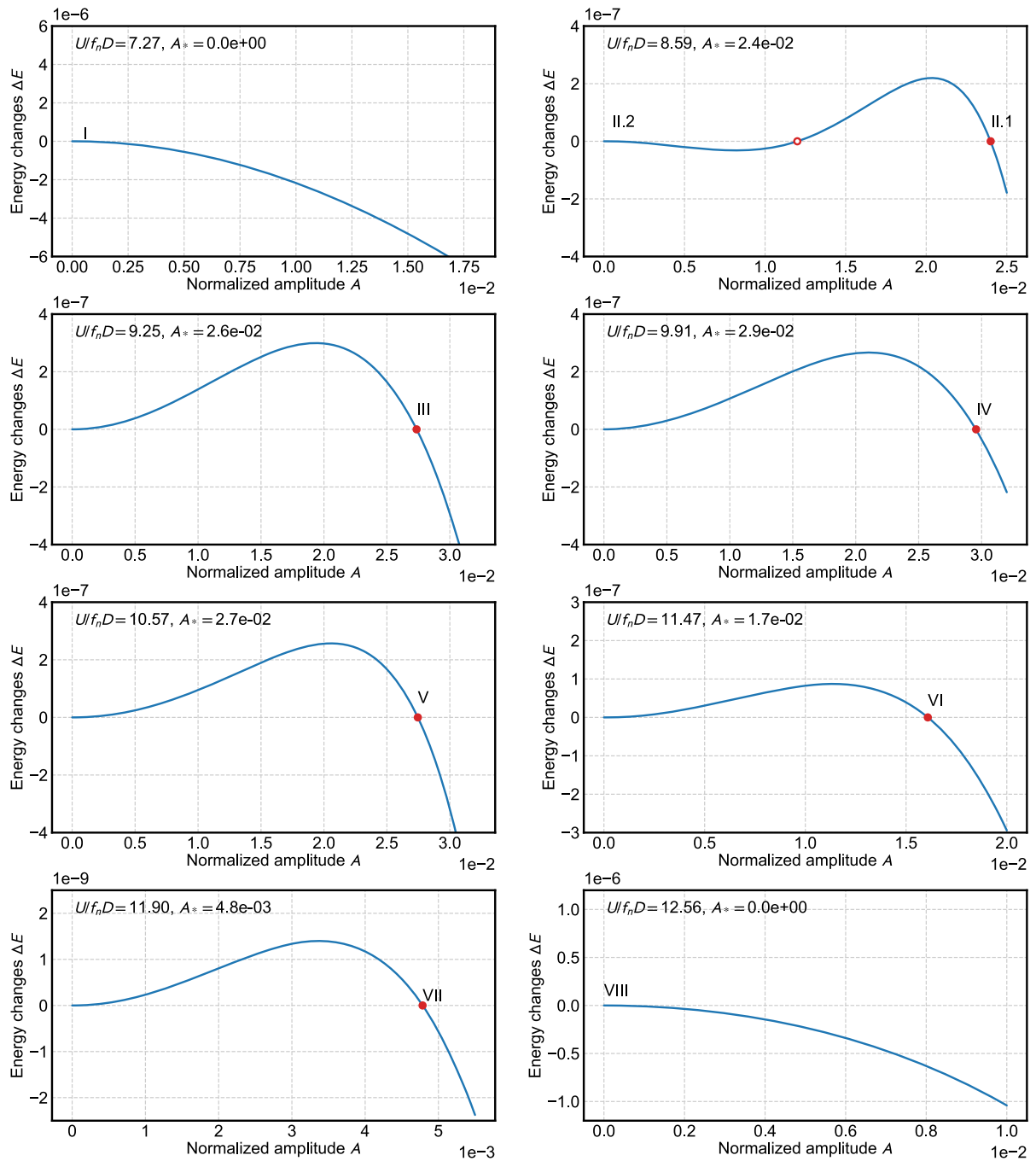
Fig. 11 1D energy map ΔE for various reduced wind speeds $U/f_n D$

6 Fluid-structural interaction stability from the perspective of "energy maps"

"Energy maps" were first introduced in [25] and [26] to identify the possible limit cycle response for the fluid–structure interaction for airfoils among different combinations of wind speeds and the amplitude of the structural response. In addition, the concept of an energy map was developed in structural engineering to analyze the progressive collapse of the old Tacoma Bridge in [14].

From a pure aeroelastic point of view, the energy extracted from a flow can be calculated by the integral of the aeroelastic power over one oscillation period.

$$\Delta E_a = \int_{\tau_0}^{\tau_0+2\pi} F_a \dot{\eta} d\tau \tag{17}$$

The ΔE_a can be produced by the synchronized measurement of the aeroelastic force and structural response simulated by computational fluid dynamics [27] or tested in the wind tunnel with a forced-motion apparatus [24].

In this study, a method is proposed to build the energy map for the VIV lock-in region based solely on the structural response. However, because structural damping is unavoidable in the suspension system in Fig. 2, the net energy ΔE is used in this study to replace the pure aeroelastic energy ΔE_a. The net energy ΔE equals ΔE_a minus the energy dissipated by damping ΔE_s

$$\Delta E = \Delta E_a - \Delta E_s \tag{18}$$

in which ΔE can be estimated by Eq. (10), and ΔE_s is calculated as $\Delta E_s = \dfrac{2\xi K_s}{v} A^2 I_0$.

Based on the parameters identified from the measurement of the VIV displacements, the relationship between the vibration amplitude A and the net energy ΔE can be calculated from Eq. (10) in the lock-in region. The net energy ΔE for a specific wind speed has only one variable: the amplitude A; therefore, it is named the 1D energy map.

Figure 11 plots the 1D energy map for various wind speeds examined in the wind tunnel tests with the known stable and unstable LCO amplitudes, as labeled in Fig. 6. It clearly shows that the amplitude of the stable LCO exactly matches the wind tunnel test results in Fig. 6, which demonstrates the accuracy of the pro-
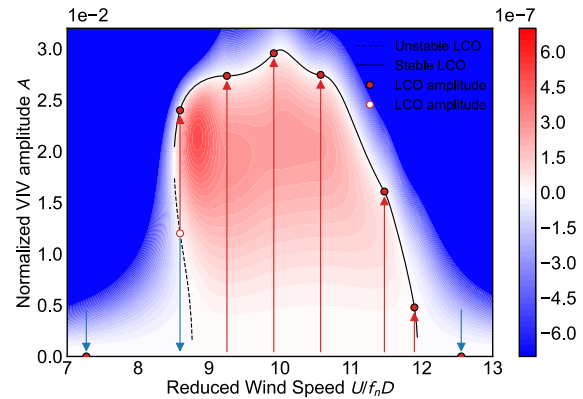
Fig. 12 Energy map for the VIV lock-in region

posed parameter identification methods based on constraint optimization. It should be noted that for large amplitudes, the energy dispassion rate will be unrealistic. If the energy map for a large amplitude is needed, the forced-motion test can be performed [14] and can be employed with a high-order polynomial aeroelastic force model.

Next, in Fig. 12, a standard energy map is constructed in Fig. 12 by interpolating the VIV parameters for various combinations of the wind speeds and amplitude. The stable LCO amplitudes tested in the wind tunnel and the unstable LCO amplitude derived from the above nonlinear dynamic model are also presented in Fig. 12. The amplitude evolution direction at different reduced wind speeds with various amplitudes is plotted as an arrowed line in Fig. 12. For engineering applications, an energy map provides a whole view of the structural equilibrium state within the lock-in region. However, it should be noted that the energy dissipation or absorption rate evaluated in Fig. 12 is determined by the generalized van der Pol model in this study. This is different from the direct measurement of the aerodynamic force in [26] and [14].

For the VIV lock-in region $8.5 < U/f_n D < 12$, the stable LCO can be calculated corresponding to the VIV amplitude found in the wind tunnel test. Additionally, for a small region for $8.5 < U/f_n D < 8.9$, there exists an unstable LCO below the stable LCO. If the initial amplitude is below the unstable LCO, the bridge deck decays to 0 since $\Delta E < 0$, while if the initial amplitude is above the unstable LCO, the bridge deck grows to a stable LCO because $\Delta E > 0$. For other lock-in regions, the bridge deck always approaches a stable LCO regardless of the initial condition.

7 Conclusions

In this paper, the multistability of bridge decks in the VIV lock-in region is studied. The traditional Scanlan's SDOF model based on the van der Pol oscillator can only predict the vibration of the bridge deck with a single stability. Moreover, a generalized van der Pol oscillation model is proposed to predict the nonlinear VIV response with multistability, in which a polynomial function of responses is employed to replace the quadratic term in Scanlan's SDOF model. Next, the averaging method is used to establish the energy change formula based on the parameters from the generalized van der Pol model. Multiple LCO amplitudes can be found by the roots of the energy-change formula. Similarly, the amplitude evolution during the transient response before reaching the LCO amplitude can also be derived from the energy change formula. Therefore, by employing multiple LCOs as an optimization constraint and transient response as an optimization target, a parameter identification algorithm based on constraint optimization is proposed. After parameter identification, 1D and 2D energy maps are constructed to illustrate the energy changes for various wind speeds and vibration amplitudes, and multiple LCOs can be observed from the energy map.

Data availibility The datasets generated and analyzed during the current study are not publicly available due to security concerns of the owner of the bridge but are available from the corresponding author on reasonable request.

Declarations

Conflict of interest The authors have no relevant financial or nonfinancial interests to disclose.

References

1. Chen, X., Kareem, A.: Coupled dynamic analysis and equivalent static wind loads on buildings with three-dimensional modes. J. Struct. Eng. (ASCE) **131**(7), 1071–1082 (2005)
2. Ehsan, F., Scanlan, R.H.: Vortex-induced vibrations of flexible bridges. J. Eng. Mech. **116**(6), 1392–1411 (1990)
3. Frandsen, J.: Simultaneous pressures and accelerations measured full-scale on the Great Belt east suspension bridge. J. Wind Eng. Ind. Aerodyn. **89**(1), 95–129 (2001)
4. Fujino, Y., Yoshida, Y.: Wind-induced vibration and control of Trans-Tokyo Bay crossing bridge. J. Struct. Eng. **128**(8), 1012–1025 (2002)
5. Gao, G., Zhu, L., Li, J., et al.: Application of a new empirical model of nonlinear self-excited force to torsional vortex-induced vibration and nonlinear flutter of bluff bridge sections. J. Wind Eng. Ind. Aerodyn. **205**(104), 313 (2020)
6. Ge, Y., Yang, Y., Cao, F.: VIV sectional model testing and field measurement of xihoumen suspension bridge with twin box girder. In: Proceedings of the 13th International Conference on Wind Engineering, Amsterdam, Netherlands, pp. 11–15 (2011)
7. Ge, Y., Zhao, L., Cao, J.: Case study of vortex-induced vibration and mitigation mechanism for a long-span suspension bridge. J. Wind Eng. Ind. Aerodyn. **220**(104), 866 (2022)
8. Grasman, J., Verhulst, F., Shih, S.D.: The lyapunov exponents of the van der pol oscillator. Math. Methods Appl. Sci. **28**(10), 1131–1139 (2005)
9. Hajj, M.R., Mehmood, A., Akhtar, I.: Single-degree-of-freedom model of displacement in vortex-induced vibrations. Nonlinear Dyn. **103**(2), 1305–1320 (2021)
10. Hartlen, R.T., Currie, I.G.: Lift-oscillator model of vortex-induced vibration. J .Eng. Mech. Div. **96**(5), 577–591 (1970)
11. Hu, C., Zhao, L., Ge, Y.: Time-frequency evolutionary characteristics of aerodynamic forces around a streamlined closed-box girder during vortex-induced vibration. J. Wind Eng. Ind. Aerodyn. **182**, 330–343 (2018)
12. Hu, C., Zhao, L., Ge, Y.: Mechanism of suppression of vortex-induced vibrations of a streamlined closed-box girder using additional small-scale components. J. Wind Eng. Ind. Aerodyn. **189**, 314–331 (2019)
13. Hu, C., Zhao, L., Ge, Y.: A simplified vortex model for the mechanism of vortex-induced vibrations in a streamlined closed-box girder. Wind Struct. **32**(4), 309–319 (2021)
14. Hu, C., Zhao, L., Ge, Y.: Wind-induced instability mechanism of old Tacoma Narrows Bridge from aerodynamic work perspective. J. Bridge Eng. **27**(5), 04022029 (2022)
15. Hwang, Y.C., Kim, S., Kim, H.K.: Cause investigation of high-mode vortex-induced vibration in a long-span suspension bridge. Struct. Infrastruct. Eng. **16**(1), 84–93 (2020)
16. Iwan, W.D., Blevins, R.D.: A model for vortex induced oscillation of structures. J. Appl. Mech. **41**(3), 581–586 (1974)
17. Javed, U., Abdelkefi, A., Akhtar, I.: An improved stability characterization for aeroelastic energy harvesting applications. Commun. Nonlinear Sci. Numer. Simul. **36**, 252–265 (2016)
18. Kovacic, I., Mickens, R.E.: A generalized van der pol type oscillator: investigation of the properties of its limit cycle. Math. Comput. Model. **55**(3–4), 645–653 (2012)

19. Kumarasena, T., Scanlan, R., Ehsan, F.: Wind-induced motions of Deer Isle bridge. J. Struct. Eng. **117**(11), 3356–3374 (1991)

20. Larsen, A., Esdahl, S., Andersen, J.E., et al.: Storebælt suspension bridge-vortex shedding excitation and mitigation by guide vanes. J. Wind Eng. Ind. Aerodyn. **88**(2–3), 283–296 (2000)

21. Li, H., Laima, S., Ou, J., et al.: Investigation of vortex-induced vibration of a suspension bridge with two separated steel box girders based on field measurements. Eng. Struct. **33**(6), 1894–1907 (2011)

22. Li, H., Laima, S., Zhang, Q., et al.: Field monitoring and validation of vortex-induced vibrations of a long-span suspension bridge. J. Wind Eng. Ind. Aerodyn. **124**, 54–67 (2014)

23. Li, K., Han, Y., Cai, C., et al.: Experimental investigation on post-flutter characteristics of a typical steel-truss suspension bridge deck. J. Wind Eng. Ind. Aerodyn. **216**(104), 724 (2021)

24. Liu, S., Zhao, L., Fang, G., et al.: Nonlinear aerodynamic characteristics and modeling of a quasi-flat plate at torsional vibration: effects of angle of attack and vibration amplitude. Nonlinear Dyn. 1–25 (2022)

25. Menon, K., Mittal, R.: Flow physics and dynamics of flow-induced pitch oscillations of an airfoil. J. Fluid Mech. **877**, 582–613 (2019)

26. Menon, K., Mittal, R.: Aeroelastic response of an airfoil to gusts: prediction and control strategies from computed energy maps. J. Fluids Struct. **97**(103), 078 (2020)

27. Menon, K., Mittal, R.: Quantitative analysis of the kinematics and induced aerodynamic loading of individual vortices in vortex-dominated flows: a computation and data-driven approach. J. Comput. Phys. **443**(110), 515 (2021)

28. Mittal, S., Singh, S.: Vortex-induced vibrations at subcritical Re. J. Fluid Mech. **534**, 185–194 (2005)

29. Nayfeh, A.H., Mook, D.T.: Nonlinear Oscillations. Wiley, Hoboken (2008)

30. Nguyen, T., Koide, M., Yamada, S., et al.: Influence of mass and damping ratios on vivs of a cylinder with a downstream counterpart in cruciform arrangement. J. Fluids Struct. **28**, 40–55 (2012)

31. Pagnini, L., Piccardo, G., Solari, G.: Viv regimes and simplified solutions by the spectral model description. J. Wind Eng. Ind. Aerodyn. **198**(104), 100 (2020)

32. Raghavan, K., Bernitsas, M.: Experimental investigation of reynolds number effect on vortex induced vibration of rigid circular cylinder on elastic supports. Ocean Eng. **38**(5–6), 719–731 (2011)

33. Strogatz, S.H.: Nonlinear Dynamics and Chaos: With Applications to Physics, Biology, Chemistry, and Engineering. CRC Press (2018)

34. Tamura, Y., Amano, A.: Mathematical model for vortex-induced oscillations of continuous systems with circular cross section. J. Wind Eng. Ind. Aerodyn. **14**(1–3), 431–442 (1983)

35. van der Pol, B.: The nonlinear theory of electric oscillations. Proc. Inst. Radio Eng. **22**(9), 1051–1086 (1934)

36. van der Pol, B., van der Mark, J.: Frequency demultiplication. Nature **120**(3019), 363–364 (1927)

37. Wang, C., Hua, X., Feng, Z., et al.: Experimental investigation on vortex-induced vibrations of a triple-box girder with web modification. J. Wind Eng. Ind. Aerodyn. **218**(104), 783 (2021)

38. Wang, W., Wang, X., Hua, X., et al.: Vibration control of vortex-induced vibrations of a bridge deck by a single-side pounding tuned mass damper. Eng. Struct. **173**, 61–75 (2018)

39. Williamson, C., Govardhan, R.: Vortex-induced vibrations. Annu. Rev. Fluid Mech. **36**, 413–455 (2004)

40. Wu, T., Kareem, A.: An overview of vortex-induced vibration (VIV) of bridge decks. Front. Struct. Civ. Eng. **6**(4), 335–347 (2012)

41. Xu, F., Ying, X., Li, Y., et al.: Experimental explorations of the torsional vortex-induced vibrations of a bridge deck. J. Bridge Eng. **21**(12), 04016093 (2016)

42. Xu, K., Ge, Y., Zhao, L., et al.: Experimental and numerical study on the dynamic stability of vortex-induced vibration of bridge decks. Int. J. Struct. Stabil. Dyn. **18**(03), 1850033 (2018)

43. Xu, K., Bi, K., Han, Q., et al.: Using tuned mass damper inerter to mitigate vortex-induced vibration of long-span bridges: analytical study. Eng. Struct. **182**, 101–111 (2019)

44. Xu, K., Ge, Y., Zhao, L.: Quantitative evaluation of empirical models of vortex-induced vibration of bridge decks through sectional model wind tunnel testing. Eng. Struct. **219**(110), 860 (2020)

45. Xu, K., Dai, Q., Bi, K., et al.: Multi-mode vortex-induced vibration control of long-span bridges by using distributed tuned mass damper inerters (DTMDIs). J. Wind Eng. Ind. Aerodyn. **224**(104), 970 (2022)

46. Xu, W.H., Zeng, X.H., Wu, Y.X.: High aspect ratio (L/D) riser viv prediction using wake oscillator model. Ocean Eng. **35**(17–18), 1769–1774 (2008)

47. Zhang, B., Song, B., Mao, Z., et al.: Numerical investigation on viv energy harvesting of bluff bodies with different cross sections in tandem arrangement. Energy **133**, 723–736 (2017)

48. Zhang, W., Li, X., Ye, Z., et al.: Mechanism of frequency lock-in in vortex-induced vibrations at low reynolds numbers. J. Fluid Mech. **783**, 72–102 (2015)

49. Zhao, L., Cui, W., Shen, X., et al.: A fast on-site measure-analyze-suppress response to control vortex-induced-vibration of a long-span bridge. Structures **35**, 192–201 (2022)